iScience

CellPress
OPEN ACCESS

Article

An industrial demonstration study on CO_2 mineralization curing for concrete

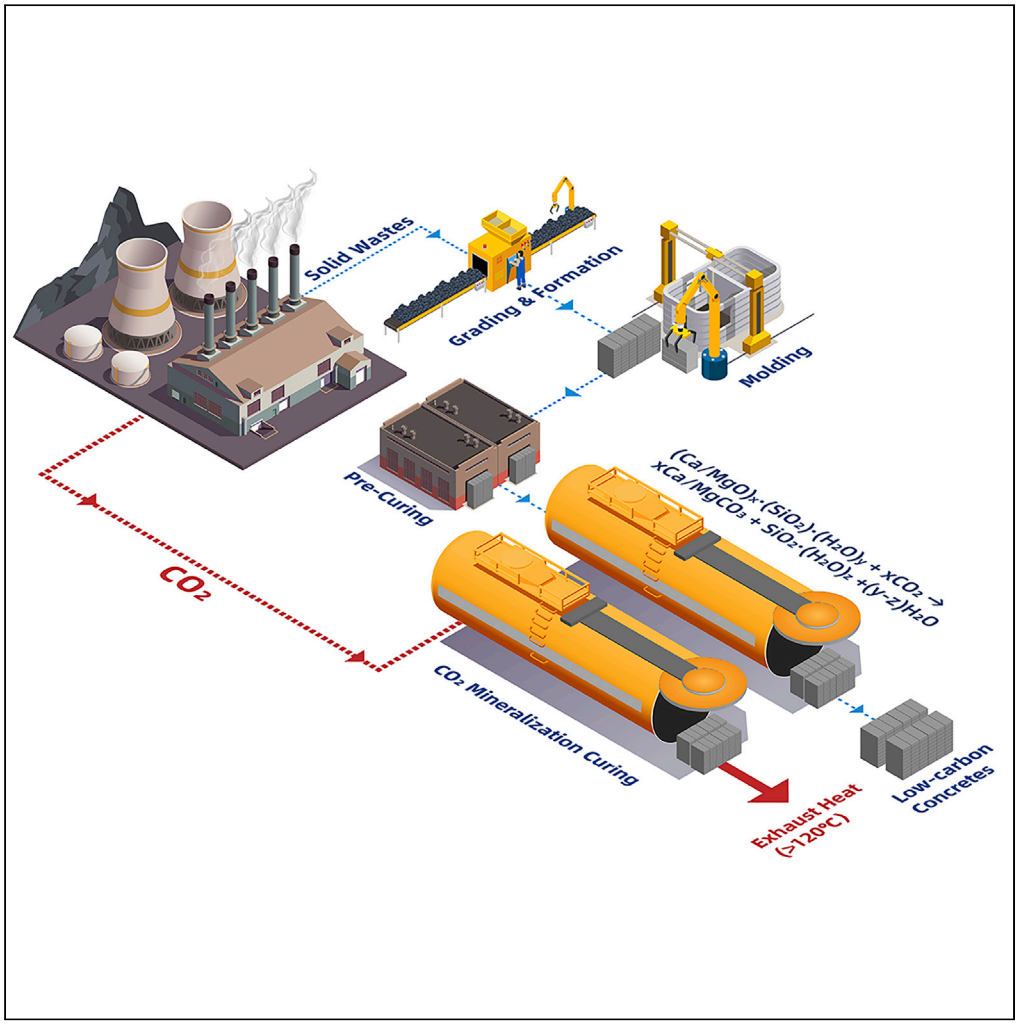

Tao Wang, Zhenwei Yi, Jiayi Song, Chao Zhao, Ruonan Guo, Xiang Gao

oatgnaw@zju.edu.cn

Highlights

A full-scale 10,000 ton/y CO_2 mineralization curing project

The CO_2 conversion rate is >98% with step pressure-equalizing process

High-temperature accumulation in industrial CMC process is first reported

The economic benefit of CMC technology is approximately 35 USD/t-CO_2

Wang et al., iScience 25, 104261
May 20, 2022 © 2022 The Author(s).
https://doi.org/10.1016/j.isci.2022.104261

iScience

CellPress
OPEN ACCESS

Article

An industrial demonstration study on CO_2 mineralization curing for concrete

Tao Wang,[1,3,*] Zhenwei Yi,[1] Jiayi Song,[1] Chao Zhao,[2] Ruonan Guo,[1] and Xiang Gao[1]

SUMMARY

A 10,000 ton-CO_2/y mineralization curing (CMC) process was demonstrated in Jiaozuo city, China by retrofitting a traditional autoclaved curing plant. An industrial concrete formula with synergistic effects of aggregate gradation, early hydration, and alkali excitation was developed using local solid wastes resources. Approximately 90% of the raw materials, including fly ash, furnace blaster slag, steel slag, and carbide slag, came from coal-based industries. An extraordinary phenomenon of high-temperature accumulation from room temperature to 140°C was first observed in an industrial scale because of the rapid and strong exothermic carbonation reaction. A step pressure-equalizing procedure was developed to achieve a rapid carbonation rate, a high CO_2 conversion ratio of >98%, and efficient carbonation exotherm recycling. The global warming potential life cycle analysis revealed that compared with autoclaved curing, CMC showed significantly decreased the emission of 182 kg CO_2-Eq/m^3-product, with direct CO_2 sequestration accounting for ~65% of the reduction.

INTRODUCTION

CO_2 mineralization uses CO_2 reactions with alkaline metals, such as calcium (Ca) and magnesium (Mg), to form stable carbonates, which is a CO_2 fixation technology with a Gibbs energy change of <0 (Xie et al., 2015) and a global sequestration potential of 10 Gt (Xie et al., 2016). *Ex situ* mineral carbonation of natural-minerals and industrial-solid-wastes has recently gained popularity due to the accelerated carbonation rate and safety (Xie et al., 2015), as well as the ability to produce various high-value products without risk of leakage.

A large amount of alkaline and neutral materials could be employed as feedstocks for *ex situ* CO_2 mineralization. Alkaline solid waste is a promising resource for CO_2 mineralization in an eco-friendly circular economy model (Monkman and Shao, 2006; Greeshma et al., 2015; Wei et al., 2018; Zhan et al., 2013, 2014). A massive amount of solid wastes (including steel slag, fly ash, and other alkaline solid wastes) is generated, especially for developing countries, presenting enormous potential for CO_2 neutrality. In China, for example, 42 million tons of CO_2 could be sequestrated via steel slag, 80.66 million tons via fly ash from coal combustion, and 8.92 million tons via carbide slag annually (Li et al., 2007; Ning et al., 2020; Xie et al., 2015, 2016).

CO_2 mineralization curing for concrete is one of the rapidly emerging technologies for large-scale CO_2 and industrial solid wastes utilization owing to the advantage of the mild condition and valuable products (Pan et al., 2012; Zhang et al., 2020; Sanna et al., 2014; Liu et al., 2021). When compared with the 4-week air curing of building materials, the cementation process via mineralization curing can be achieved under a mild condition (<80°C, 0.1–40 bar) (Huang et al., 2019a; Wang et al., 2017, 2021) and completed in a matter of hours (Wang et al., 2017). Researchers have been working on developing flexible formulas, such as Wollastonite-Portland cement (He et al., 2020; Huang et al., 2019a; Wang et al., 2017), MgO-Portland cement (Vanderperre and Al-Tabbaa, 2007; Wang et al., 2020), Slag-Portland cement (Li et al., 2020a; Mo et al., 2016; Yi et al., 2020), and waste concrete aggregate (Liang et al., 2020; Tang et al., 2020; Zhan et al., 2013, 2016). However, for different products, the cumulative energy demand (CED-NRe) of the process varies between 2,000 and 4,000 MJ/m^3 product (Huang et al., 2019b), which is highly dependent on the raw materials selection and source (Kim et al., 2013; Wang, 2020), preparing processes (Huijgen et al., 2007; Huijgen et al., 2006; IEA, 2013), and curing system (Liu et al., 2021). Furthermore, the performances (the level of density and compressive strength) of the products determine the economic benefits of the whole process. Thus,

[1]State Key Laboratory of Clean Energy Utilization, Zhejiang University, China

[2]Clean Carbon (Beijing) Technology Co., Ltd, Beijing, China

[3]Lead contact

*Correspondence: oatgnaw@zju.edu.cn

https://doi.org/10.1016/j.isci.2022.104261

This is an open access article under the CC BY-NC-ND license (http://creativecommons.org/licenses/by-nc-nd/4.0/).

the challenge of process designs is to balance the competing demands of high product performance, low energy consumption, and high efficiency of carbon sequestration efficiency.

CMC technology was determined to be TRL-8 stage (NASA, 2012), and corresponding industrial tests have been conducted gradually for demonstration by different groups such as CarbonCure, CarbonBuilt, and Carbicrete. More than 1 Gt/y industrial solid waste was reused in China to produce building materials (Commission, 2014), such as autoclaved fly ash block, precast concretes, and aggregates. This study proposed a set of operational CMC processes and reported a 10,000-ton/y CO_2 concrete curing demonstration in central China. Relevant results are provided in the following sections, including curing condition optimization, process design, continuous operation, product physicochemical characterization, and material and heat balance analysis. The net CO_2 sequestration rate was evaluated through life cycle analysis (LCA), and the levelized cost of CO_2 concrete was also reported.

Technology and process description

CO_2 mineralization curing

The industrial scale CMC demonstration has sufficient technical theory support. The accelerated carbonation in chamber reactor is happened by the reaction of mid-pressure CO_2 and alkali metal (Ca/Mg) in Ordinary Portland Cement (OPC)-based (Equation 1) and solid-wastes-based (Equation 2) materials. Different from the natural carbonation of building materials, concrete treated with CMC technology has higher carbonation depth associated with the enhanced performances.

$$(CaO)_x \cdot SiO_2 + xCO_2 + nH_2O \rightarrow SiO_2 + nH_2O + xCaCO_3 \quad \text{(Equation 1)}$$

$$(Ca/MgO)_x \cdot (SiO_2) \cdot (H_2O)_y + xCO_2 \rightarrow xCa/MgCO_3 + SiO_2 \cdot (H_2O)_z + (y - z)H_2O \quad \text{(Equation 2)}$$

In the CMC technology system, CO_2 gas molecules diffuse through the micropore structure of the formed concrete and finally, fast react with the carbonated active component to form the stable $CaCO_3$ microcrystal. The concrete microstructure is significantly affected by carbonation process, which is manifested by the two side effects: (1) the filling effect by carbonation production of $CaCO_3$ microcrystal; (2) the carbonation cementitious effect improves the interface transition zone (Wang et al., 2017). In addition, the carbonation kinetics can be improved through significant interface continuity by adjusting the doping ratio of inert substances in the concrete system (Huang et al., 2019a). Therefore, kinetically, the CO_2-diffusion-controlled carbonation process can be enhanced by active controlling of the CO_2 partial pressure (Huang et al., 2019a; Wang et al., 2017; Yi et al., 2020).

The curing process is generally operated at room temperature; there is no need for the extra heat resource compared with the traditional autoclaved curing. Due to carbonation reaction heat release, the temperature rise could improve the gas diffusion and carbonation reaction kinetics (Zhan et al., 2013; Wang et al., 2021). Because the decomposition temperature of carbonates in concrete is >400°C (Khan et al., 2021), thermodynamically, the negative effect of heating process on CO_2 sequestration is negligible during CMC process.

Industrial demonstration process

CMC process was supported by a fully equipped system retrofitted based on a traditional autoclaved curing plant in Henan Qiangnai New Materials Co., Ltd. Annually, the factory produces 200,000 tons of the block using a traditional autoclaved curing process, consuming 9,000 tons of steam and 630,000 m^3 of natural gas.

The whole CMC system comprised filler blender unit, mandatory broken unit, brick machine unit, pre-curing room unit, CO_2 curing chamber unit, gasification pry unit, and packaging and transportation unit (Figure 1). The raw materials, including coarse aggregate (slag), fine aggregate (ash), and cementitious material (cement), were first fed into the bin feeders in the appropriate proportion, aggregate gradation, and water to solid ratio. After stirring in the blender, the filler mixture was transferred to the mandatory broken unit, which was molded in the brick machine unit and distributed into the cubic mold after oscillating in the brick machine. Following a pre-curing process (natural condition), the ready brick was sent to the CO_2 curing workshop for CO_2 mineralization curing. The performance parameters of each unit are summarized in Table S1.

The CO_2 gas used in this study was supplied from the liquid-CO_2 tanker. A gasification system, with a capacity of 500 m^3/h (in 1.2 MPa and 20°C) and an electric auxiliary heat device was employed to provide a consistent supply of gaseous CO_2 to the curing chamber. The step pressure-equalizing (PE) CO_2 curing procedure was applied in

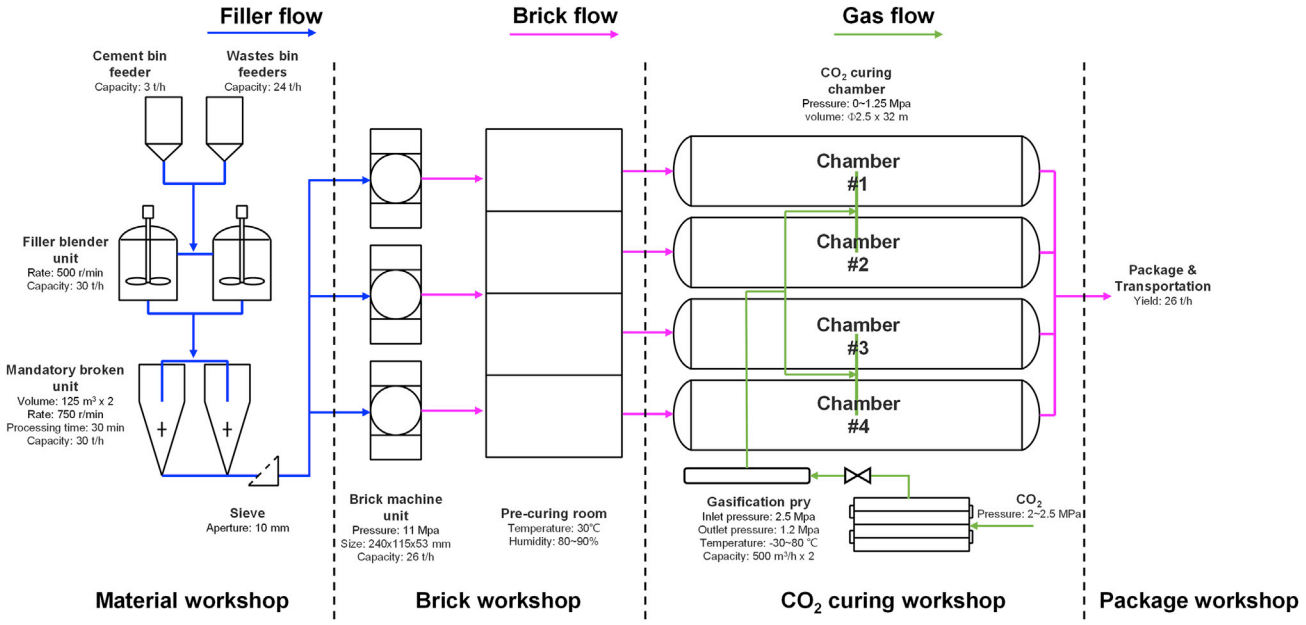

Figure 1. Schematic diagram of CMC process

this CMC demonstration to recycle the majority of the CO_2 gas. For a one-step PE operation, after the curing process in chambers #1, #2 was completed with gas pressure P_1; chambers #1, #2, #3, and #4 were connected via a gas separate cylinder, and the pressure was equalized to P_2. At least half of the gas in chambers #1 and #2 were recycled to chambers #3 and #4 during the PE process. Following the PE operation, the residual gas in chambers #1 and #2 were evacuated to the atmosphere, followed by the unloading of concrete products from the chambers.

RESULTS

Optimization of pre-curing process

The pre-curing process allows the block to undergo early hydration process, which influences the performance of CO_2 mineralization, particularly CO_2 uptake and compressive strength. The actual size sample (240 mm × 115 mm × 53 mm) and a smaller reactor (~600L) were used in laboratory to optimize the pre-curing process. As demonstrated in Figure 2, as the pre-curing time is increased, the residual w/s decreases due to the water evaporation. A rapid water loss was observed in the first 24 h, accounting for more than 70% of the total water loss. CO_2 uptake had a noticeable negative relationship with the residual w/s, which was attributed to changes in gas permeability in concrete blocks (Wang et al., 2017; Huang et al., 2019a; Yi et al., 2020). CO_2 mineralization reactions accompanied by early hydration could result in denser microstructure and strength enhancement (Guo et al., 2019; Greeshma et al., 2015; Jang et al., 2016), demonstrating a positive correlation of compressive strength with CO_2 uptake. Considering the improvement of CO_2 mineralization performance and pre-curing efficiency, the optimal water loss could be controlled at 4–5 wt.% with a pre-curing time of about 24 h. Further increase in the water loss may cause serious concrete shrinkage (Li et al., 2020b) and decrease production efficiency.

Performance of CO_2 curing

Temperature and pressure evolution in the CO_2 curing chamber

Figures 3A and 3B depict the temperature and pressure evolution in the CO_2 curing chamber (~150 m^3) within 72 h, which included nine cycles of CO_2 curing and 8 times of PE operation. It took about 6–7 h for gas intake and pressure to rise for each cycle. The chamber pressure dropped dramatically during the PE stage, from 0.6–0.7 MPa to 0.05–0.1 MPa, in 20–30 min. This is because the fresh concrete in the next group of chambers provided a high-adsorption driving force owing to the high mineralization kinetics in the initial stage (Wang et al., 2017; Huang et al., 2019a; Guo et al., 2019; Yi et al., 2020). In addition, the low residue CO_2 pressure would result in a high CO_2 conversion ratio. Meanwhile, an intriguing phenomenon of dramatic temperature rise was observed inside the curing chamber. The heat released by the carbonation reaction caused the chamber temperature to rise above 100°C. The highest curing temperature reached was over 140°C.

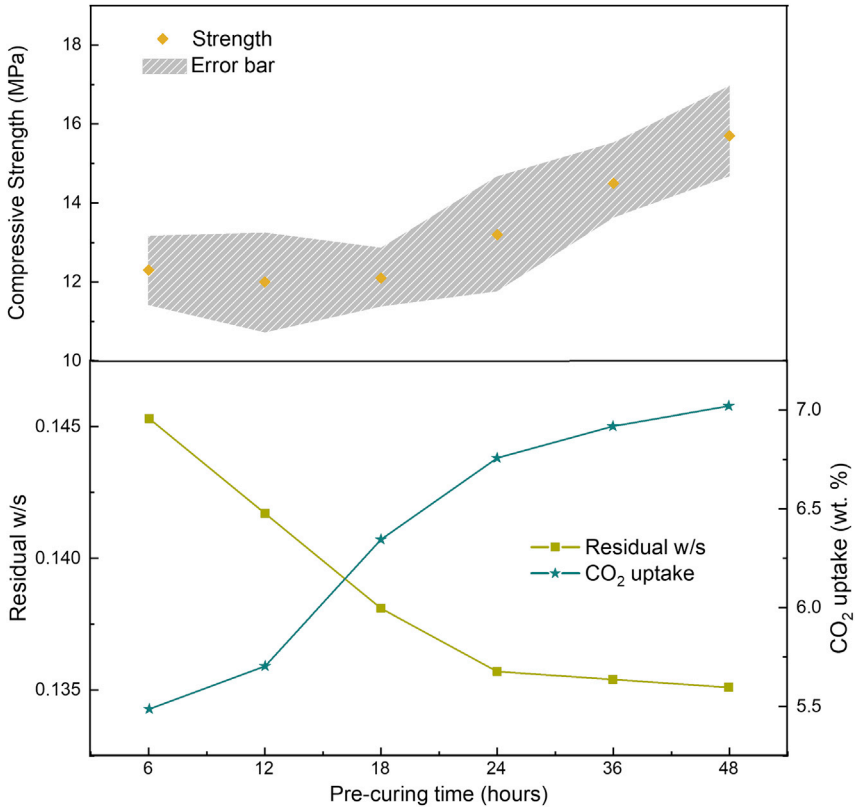

Figure 2. Effect of pre-curing time on residual w/s, CO_2 uptake, and compressive strength
(initial w/s = 0.18, 25°C, 4 h curing with 99% purity of CO_2).

As an example, in the PE stage of a single curing cycle (Figure 3C), approximately 3 tons of CO_2, or 50% of the total gas intake, was consumed in 30 min with the temperature increased to 45°C. The pressure plateau indicates a fast mineralization process during the early period of external gas supply (30–120 min). At the same time, because the majority of the carbonation reaction heat can be stored in high heat capacity bricks, the temperature also performed a plateau of about 90 min. The pressure dropped markedly during the gas-stop stage (350–430 min) without external gas intake, but the temperature kept rising, indicating that the concrete still had high reaction activity after 6 h of carbonation process.

Evaluation of CO_2 curing kinetics

According to the CO_2 curing kinetics (Figure 4A), the fastest carbonation happens during the PE stage. The CO_2 uptake rate reached to 36 t/h in the very initial stage. In chambers #5 and #6, 60% of CO_2 was adsorbed in 30min. Further analysis revealed that the CO_2 uptake rate was controlled by the gas equalizing rate, as the slops of cures are close to 1 (Figure 4B). The steadily increasing CO_2 uptake in the external gas supplying stage demonstrated a nonstop carbonation reaction lasting up to 450 min. The paralleled fitting curves in Figure 4C show that the CO_2 uptake rate is kept around 0.02 t-CO_2/min, slightly less than the gas intake rate (0.022–0.035 t-CO_2/min). This phenomenon supports the hypothesis of product layer diffusion-controlled kinetics (Wang et al., 2017; Huang et al., 2019a; Yi et al., 2020), which is attributed to the fast densification effect of the carbonation reaction on the concrete surface.

Performance characterization of CO_2 concrete

CO_2 uptake

During the 72-h continuous curing operation, 101 tons of CO_2 were supplied to the system, and 1.04 tons of residual CO_2 were released to the atmosphere after pressure equalization, yielding a CO_2 conversion rate of 98.97%. The annual CO_2 sequestration at this capacity is approximately 11,000 tons (running 8000 h/year) with 5.3 wt.% CO_2 uptake of concrete. Blocks at different spatial positions in the cross-section of the curing

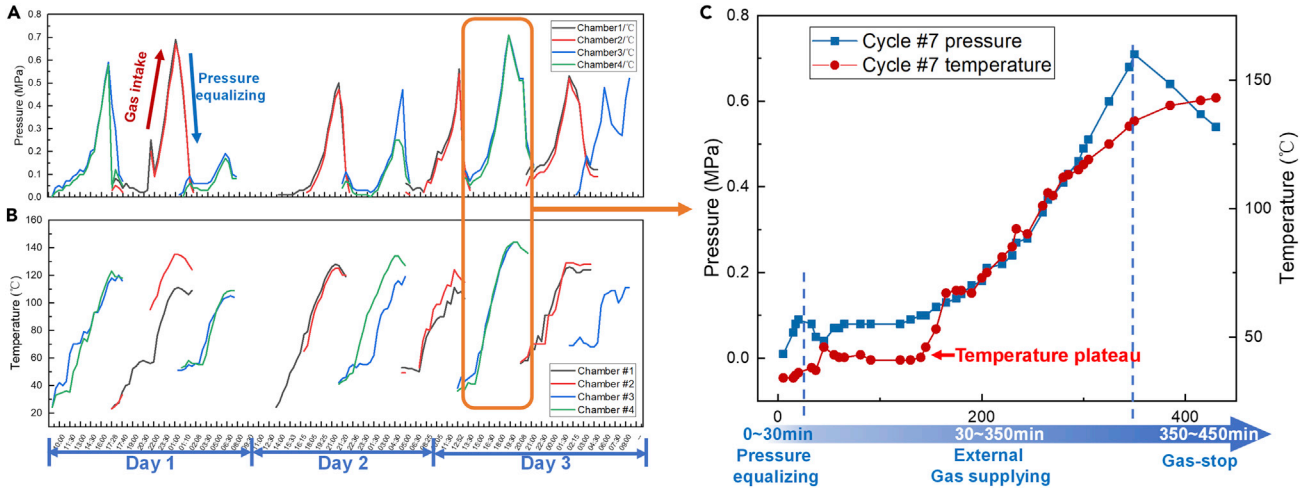

Figure 3. Pressure and temperature change within 72 h

(A) Pressure; (B) temperature; (C) pressure and temperature change of chamber #4 in the seventh curing cycle.

chamber (Figure 5A) were sampled to investigate the difference in CO_2 uptake. The CO_2 uptake value and phenolphthalein cross-section test showed that the carbonation depth of bricks was increased from 0.5 cm to 2.5 cm from the top position to the bottom position. The TGA results in Figure 5B illustrate the significant difference of CO_2 uptake for bricks at a different position inside the chamber. This intriguing phenomenon is thought to be related to the uneven CO_2 concentration distribution in the chamber. The partial pressure of CO_2 in the lower part of the chamber may be higher because of the relatively lower position of CO_2 inlet and higher density of CO_2 gas as compared with the density of air.

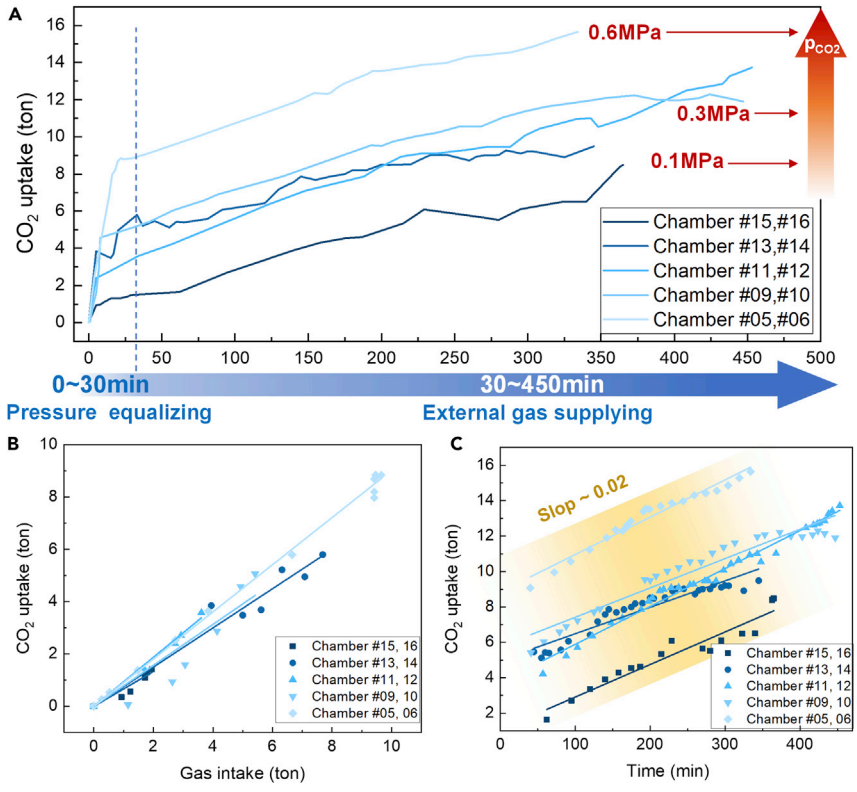

Figure 4. CO_2 uptake kinetic analysis of CO_2 curing process

(A) The whole stage, (B) PE stage, and (C) external gas supplying stage.

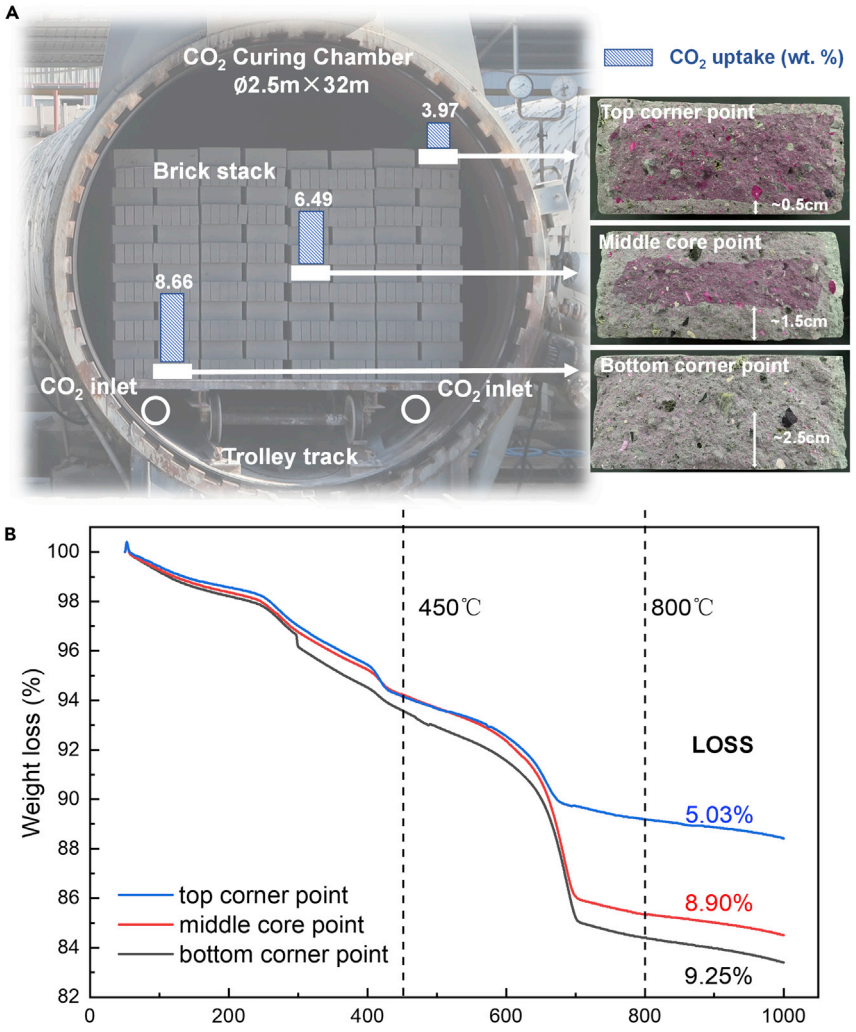

Figure 5. CO_2 uptake of different spatial positions

(A) Phenolphthalein test and (B) TG test results on different spatial positions.

Compressive strength

The compressive strength of bricks as shown in Figure 6A can be used to characterize the practical mechanical performance. The significant improvement in compressive performance due to CO_2 curing could be attributed to the densification effect (Wang et al., 2017; Tang et al., 2020) of carbonation, which helped strengthen the microstructure. Because of the later hydration, the compressive strength could reach to 15 MPa after 1 week and increased to more than 20 MPa over the next 4–5 weeks, with a 70.5% strength enhancement compared with the samples that did not receive CO_2 curing. The longer-lasting later hydration effect may be attributed to the denser product layer formed by carbonation, which has a higher water-retention property. As demonstrated in Figure 6B, the compressive strength was noticeably affected by spatial position. The densification effect during carbonation should increase the compressive strength with increased CO_2 uptake, which is consistent with the pattern found in laboratory experiments in Section "Optimization of pre-curing process."

Microscale characterization of carbonation product

Chemical composition

Because SiO_2 is a relatively stable component, the carbonation degree of bricks could be semiquatitatively analyzed by using the ratio of relative characteristic peak intense of $CaCO_3$ to SiO_2. As illustrated in Figure 7A, the relative peak height of carbonation product $CaCO_3$ (~29.5°) increased significantly after CO_2 mineralization

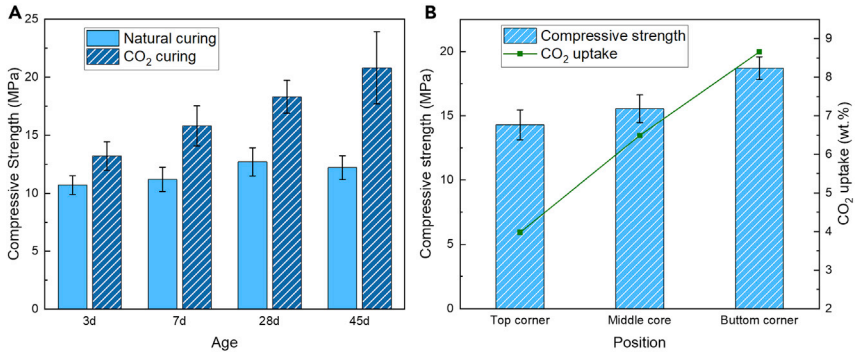

Figure 6. Compressive strength of bricks
(A) Different age and (B) different spatial position.

curing. Meanwhile, the hydration products $Ca(OH)_2$ (~17.5°) and carbonation product $CaCO_3$ (~29.5°) were gradually increased with an increase in pre-curing time (24–48 h) after CO_2 curing. According to the relative peak height of $CaCO_3$ in Figure 7B, the higher the chamber temperature, the more the $CaCO_3$ was generated, indicating that the carbonation reaction of concrete is primarily controlled by kinetics below 150°C. At the same time, the carbonation conversion rate is far from reaching the thermodynamic maximum.

Microstructure

Compared with the regular rod-like $Ca(OH)_2$ crystal observed during the normal hydration process (Figure 8A), more calcium-modified silica gel was formed during 104°C CO_2 curing, which may be due to the alkali excitation effect at high temperatures (Gómez-Casero et al., 2021; Aydın and Baradan, 2012) (Figure 8B). Carbonation products tended to form aragonite crystal and metastable vaterite rather than calcite as carbonation temperature increased (Figures 8C and 8D). Vaterite, a rare carbonation product in concrete, was only observed when the carbonation temperature exceeded 140°C. It is well known that vaterite is a metastable polymorph with the highest energy level of the three typical $CaCO_3$ morphologies and that it is formed in a moist environment at high temperatures (>100°C) (López-Arce et al., 2011; Bjørge et al., 2019). Therefore, one can infer that CO_2 curing at relatively high humidity and temperature could elevate the energy level of $CaCO_3$ carbonation products and form relatively unstable polymorphs (aragonite and vaterite) (Bjørge et al., 2019; Wang et al., 2019).

Mass balance and benefit analysis

Mass and heat balance analysis

In this demonstration, the boundary of the materials balance calculation was deposited as a single process line from raw materials (slag, ash, cement, and gaseous CO_2) into the factory to the finished brick (light low-carbon concrete brick) out of the factory (Figure 9). During the 72-h demonstration, 1909 tons of materials were consumed, containing 50% of slags, 40% of ashes, and 10% of cement. Analysis of the change of water content in bricks revealed that the water evaporation during pre-curing was 26.22 tons. During the curing process, the CO_2 intake during the 72-h test was 101 tons as determined by weighing the CO_2 tank truck.

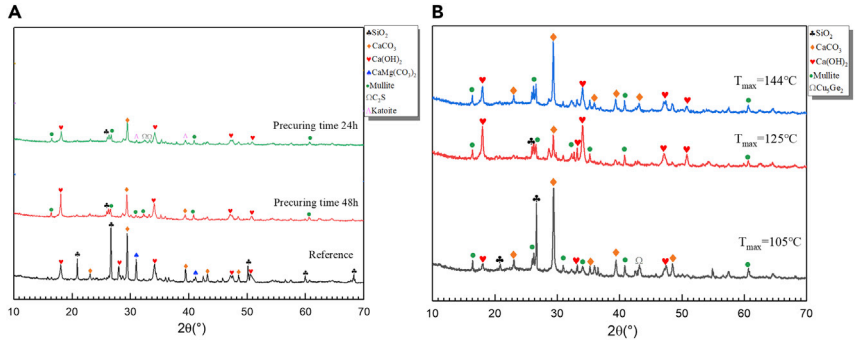

Figure 7. XRD analysis of bricks
(A) Different pre-curing times and (B) different maximum curing temperatures.

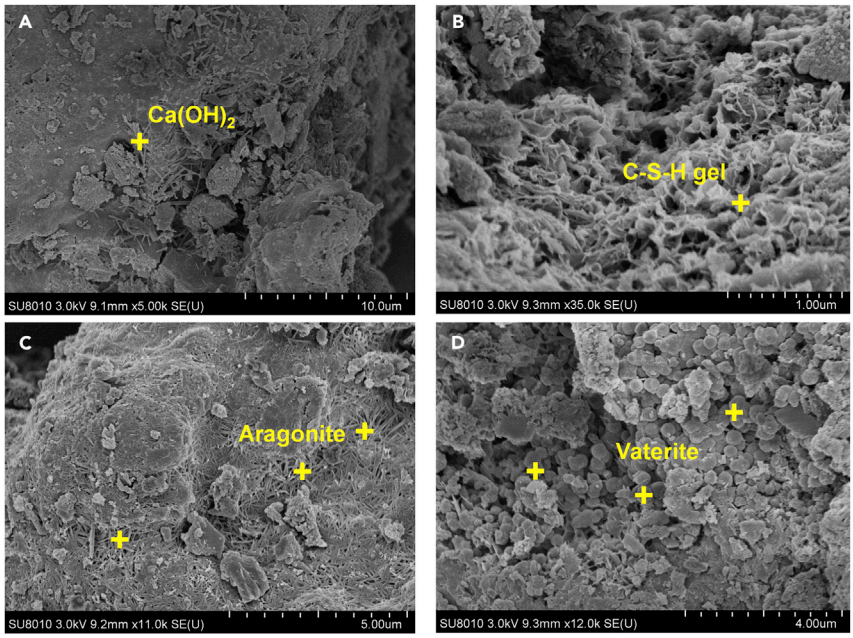

Figure 8. SEM pictures of bricks

(A) Natural curing; (B) CO_2 curing (max temperature = 104°C); (C) CO_2 curing (max temperature = 125°C); (D) CO_2 curing (max temperature = 144°C).

Moreover, the residual CO_2 was calculated as 1.04 tons using Equation 4, whereas the CO_2 conversion rate was 98.9% (see Table S2). Water evaporation and precipitation (average moisture content change of bricks before and after curing) were calculated to be 39.06 tons during the CO_2 curing process.

Figure 10 illustrates the Sankey plot of mass and heat flow during a curing period, based on the data from a typical curing chamber. The heat release was calculated using the HSC CHEMISTRY 6.0 reaction enthalpy database (see Table S3) and Equation 7. The total heat of the carbonation reaction was approximately 18.6 GJ, as the only heat source of the entire process. The sensible heat of solid and water in bricks dominates the heat flow, accounting for 57.5% and 16.7% of the total, respectively. The sensible heat of steel (chamber body and trolley), the heat dissipation, and latent heat of exhausted steam each accounted for 18.6%, 5.9%, and 1.2% of total heat, respectively.

Carbon LCA analysis—global warming potential

Considering the low reactivity of the block with CO_2 after CMC and autoclave curing (The low free-CaO content in Table S4), passive CO_2 absorption during the lifetime of the block was not calculated in this paper. Therefore, the "cradle to gate" is set as the LCA calculating boundary (ISO 14040 &14044) for the whole system, and the detailed boundary schematic diagram is shown in Figure 11. The raw material and external input GWP data were obtained from the world's life cycle inventory (LCI) database—ecoinvent 3.7 (Sep. 2020) (Ecoivent, 2020). The database is

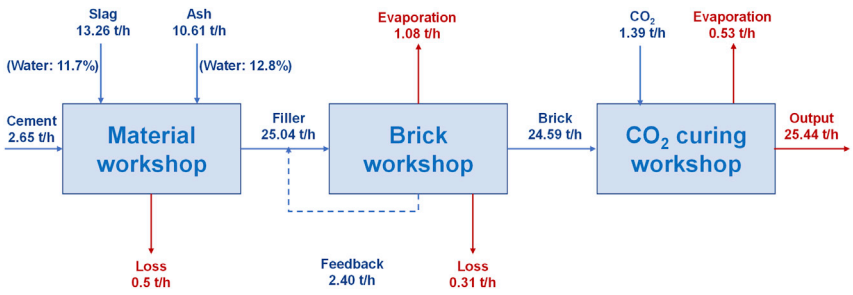

Figure 9. Materials flow balance schematic of CMC process

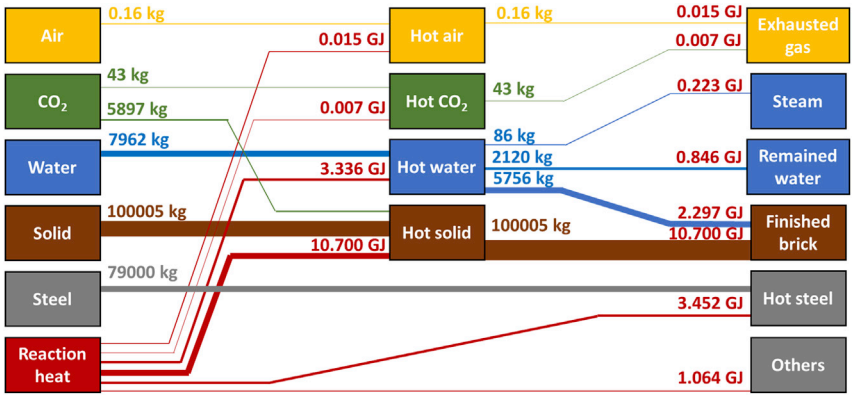

Figure 10. Sankey plot of mass and heat balance analysis in the CO_2 curing chamber

now known as the largest LCI database, containing data from statistical and published technical literature. Figure 11 illustrates the allocation of resource input units for various industrial activities. The electric power emission data were obtained from the ecoinvent database based on the power source in Henan province, China; coal and diesel were based on global average emissions.

Figure 12 shows a significant difference in GWP between CO_2 curing and autoclaved curing (Detailed calculation is provided in Table S5). Blocks with the same strength level (>15 MPa) are used for GWP analysis of different processes. The GWP of the CMC process is 58.51 kg CO_2-Eq/m^3, which is only 1/4 of the autoclaved curing process (241.30 kg CO_2-Eq/m^3). The vast differences were primarily due to the differences in material formulation and CO_2 sequestration capacity between the two processes. The majority of CO_2 emissions in raw materials came from cement manufacturing, making the GWP highly dependent on concrete mixture design. Therefore, using of industrial solid waste instead of cement significantly reduced GWP and also allows the solid-waste-based concrete to achieve a lower GWP index in the raw material unit. The contribution of transportation to GWP is negligible (less than 2%), and it is unaffected by changes in raw material freight volume distribution. GWP did not differ significantly at the end of manufacturing process because the processes of CO_2 curing and autoclaved curing were similar. Moreover, when compared with autoclaved curing, CO_2 curing had a significant carbon-negative effect with a GWP of −120 kg CO_2-Eq/m^3.

Technical economic analysis

The boundary, functional units, and allocations of technical economic analysis (TEA) were based on the LCI calculation for GWP provided in STAR Methods and Table S6. Of note, transportation costs are factored into raw materials prices. As demonstrated in Figure 13, the operational cost of the CMC process was 30.93 USD/m^3, with raw material (74.25%), manufacture (8.23%), gas supply (9.42%), and labor (8.10%). Compared with the autoclaved curing process, CMC effectively reduced the proportion of cement in raw materials with a cost advantage of 2.09 USD/m^3. A similar process structure resulted in comparable costs of manufacturing and labor. The cost of CO_2 gas supply based on PSA (Union_Engineering, 2016) was, however, higher than that of steam.

Considering the local production (lightweight concrete brick) price (~36.3 USD/m^3), the economic benefits of the two processes are 5.40 USD/m^3 for CO_2 curing and 5.31 USD/m^3 for autoclaved curing. Notably, the product capacity of CO_2 curing (6–8 h/cycle, as shown in Figure 5) is more than 1.5 times that of autoclaved curing (8–12 h/cycle), which can increase the plant revenues by more than 50% per year. As a CO_2 utilization technology, the negative cost benefit of CMC technology can reach 45 USD/t-CO_2 without a carbon tax. In addition, when integrated with existing coal-fired flue gas CO_2 capture at ~40 USD/t-CO_2, CMC technology still has a high economic benefit of ~35 USD/t-CO_2.

DISCUSSIONS

Uncertainty analysis

LCA uncertainty

As shown in the table in Figure 14, two scenarios are set up to predict the influence of potential changes in CMC process on GWP index. In the two scenarios, cement content, transportation distance, manufacture

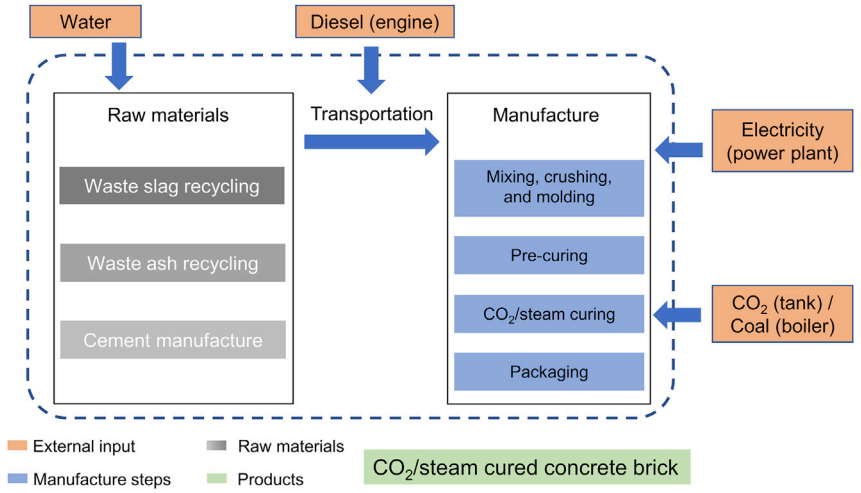

Figure 11. LCA calculation boundary

energy consumption, and CO_2 uptake are set as ±50% of the base scenario. The GWP of cement in raw material is still dominant (201 kg CO_2-eq in negative and 67 kg CO_2-eq in positive), and the resulting change (Wang et al., 2017) in CO_2 uptake (−180 kg CO_2-eq in negative and −60 kg CO_2-eq in positive) does not compensate for the emission. Although the sightly emission change in transportation distance is negligible to the GWP of CMC process, increasing transportation distance still elevates the raw material cost (from TEA). Therefore, a >50% GWP reduction can be achieved in the future by positively reducing cement content, optimizing CO_2 uptake, and manufacture energy consumption by the deployment of renewable energy.

TEA uncertainty

The potential green premium for CMC technology can be obtained through the incentives from carbon trading by recycling CO_2 and operational cost reduction from renewable energy deployment. Hence, we use the most competitive price index ($/m^3-Block) to measure the future economics of CMC technology (Figure 15). Based on the TEA data, a Cost-Price model was established to analyze the future changes of block price. For concrete manufacturers using CMC technology, the decision on minimum pricing can be made in combination with carbon tax under the premise of ensuring income (5.4$/m^3-Block).

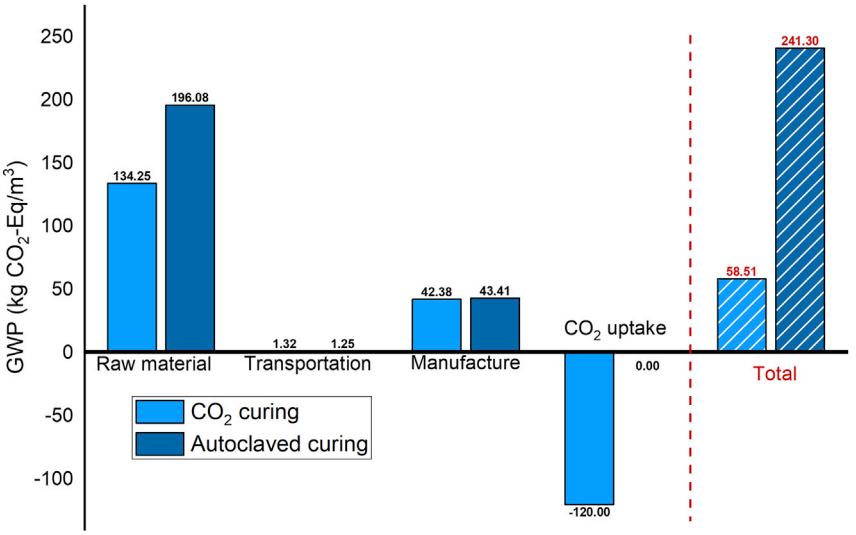

Figure 12. The GWP indicator results for CO_2 curing and autoclaved curing processes

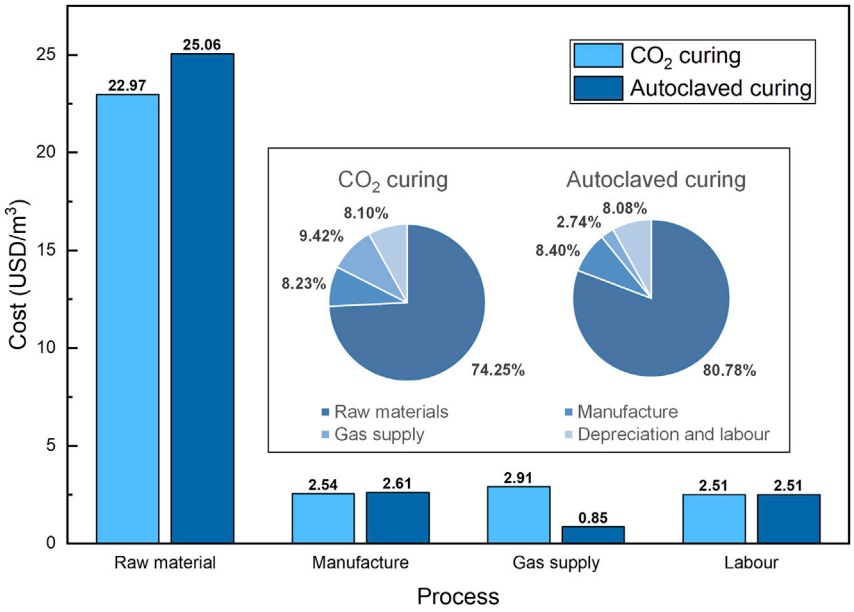

Figure 13. The operational cost of CO_2 curing and autoclaved curing processes

The operational cost of CO_2 curing and autoclaved curing processes.

Before the large-scale deployment of renewable energy, the contribution to operational cost reduction is limited, but the incentives from carbon trading will help concrete manufacturers quickly reap the benefits (blue line in Figure 15). Suppose in the future carbon trading scenario (Reference from: European Union Allowance, EUA ~100 $/t-$CO_2$ (ESMA, 2021)), compared with the traditional autoclaved curing process, CMC can achieve ~$12/t-Block of benefits through negative carbon benefits, which is equivalent to a 1/3 reduction in operational cost. In the scenario of large-scale deployment of renewable energy, if the operational cost reduced by 50% by getting cheaper raw materials, manufacturers can still benefit from CMC technology even if the blocks do not enter the market (Price = 0).

Contribution of this study

This industrial CMC process demonstrates the vast demand for industrial solid waste from the block defined as a "low-carbon" building material. This study discusses the adaptability of raw materials and product property index, which helps wider audience to have a concrete concept of low-carbon building materials from the preparation method and product performance.

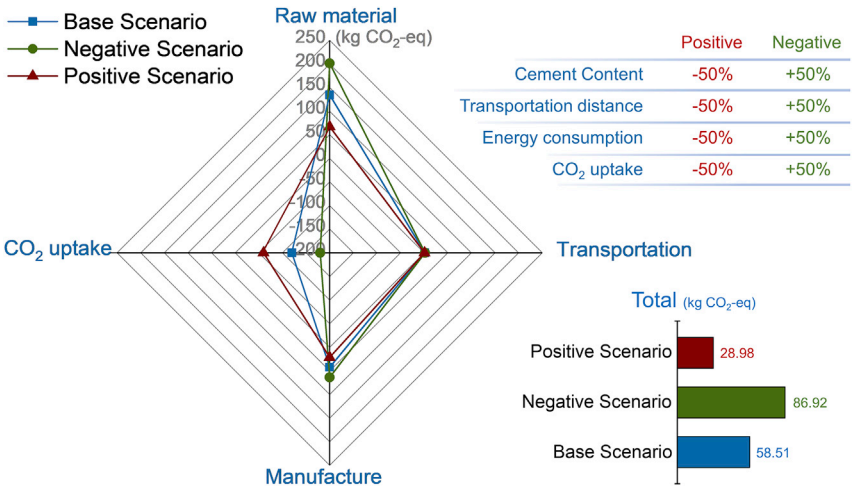

Figure 14. Scenario modeling of GWP in CMC process

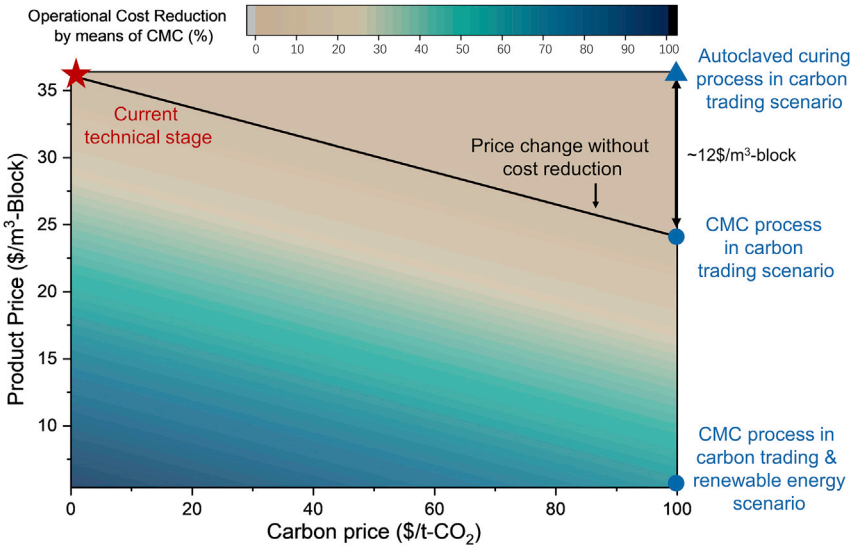

Figure 15. Green premium analysis for CMC technology

In the study of CO_2 curing kinetics at the industrial scale as mentioned in Section "Performance of CO_2 curing," favorable product performances can be obtained at different CO_2 partial pressures (from 0.1 MPa to 0.6 MPa). This demonstrates that a flexible carbon source choosing can be realized by combining CMC with impure CO_2 gas from cement mill, steel mill, and coal chemistry factory upstream. This helps to make CO_2 more valuable for developing countries to form a huge carbon sink close to the source of CO_2 emissions.

A full-scale CMC industrial demonstration provides a set of complete process parameters, mass and heat balance data, LCA data, and TEA data for assessment by the third party, which help in the future industrial design.

Limitations of the study

In actual industrial application, CO_2 may come from a variety of scenarios (flue gas CO_2 of ~12% from coal-fired power plant or high concentration CO_2 from coal chemistry). Therefore, it is worth to study the integration process of CMC and different CO_2 gas sources and explore the potential cost reductions. In the future, CMC technology should be compatible with a wider range of building material product orientation (precast concrete unit, ready-mixed concrete, and aggregates). It is necessary to systematically study the technical process, product performance, LCA, and TEA of different building material products through more demonstrations.

STAR★METHODS

Detailed methods are provided in the online version of this paper and include the following:

- KEY RESOURCES TABLE
- RESOURCE AVAILABILITY
  - Lead contact
  - Materials availability
  - Data and code availability
- METHOD DETAILS
  - Raw materials
  - Physicochemical characterization
- QUANTIFICATION AND STATISTICAL ANALYSIS
  - Calculating methods
  - Calculation of LCI
  - Calculation of economic benefit

SUPPLEMENTAL INFORMATION

Supplemental information can be found online at https://doi.org/10.1016/j.isci.2022.104261.

ACKNOWLEDGMENTS

This work was supported by the National Key R&D Program of China (grant number 2018YFB0605704), Zhejiang Provincial Natural Science Foundation of China (grant number LR19E060002), and Fundamental Research Funds for Zhejiang Provincial Universities (grant number 2021XZZX012). The authors also thank the support received from the Henan Qiangnai New Materials Co., Ltd.

AUTHOR CONTRIBUTIONS

T. W.*: Project administration, Supervision, Visualization, Writing—Reviewing, and Editing; Z. W. Y.: Investigation, Formal analysis, Conceptualization, Methodology, Software: Data curation, Writing—Original draft preparation, Writing—Reviewing, and Editing; J. Y. S.: Resources, Formal analysis, Methodology, Reviewing, and Editing; C.Z.: Resources, Reviewing, and Editing. R. N. G.: Resources, and Reviewing; X. G.: Reviewing.

DECLARATION OF INTERESTS

The authors declare no competing interests.

Received: December 17, 2021
Revised: March 28, 2022
Accepted: April 11, 2022
Published: May 20, 2022

REFERENCES

Aydın, S., and Baradan, B. (2012). Mechanical and microstructural properties of heat cured alkali-activated slag mortars. Mater. Des. *35*, 374–383. https://doi.org/10.1016/j.matdes.2011.10.005.

Bjørge, R., Gawel, K., Chavez Panduro, E.A., and Torsæter, M. (2019). Carbonation of silica cement at high-temperature well conditions. Int. J. Greenhouse Gas Control *82*, 261–268. https://doi.org/10.1016/j.ijggc.2019.01.011.

Chen, C., Habert, G., Bouzidi, Y., Jullien, A., and Ventura, A. (2010). LCA allocation procedure used as an incitative method for waste recycling: an application to mineral additions in concrete. Resour. Conserv. Recycl. *54*, 1231–1240. https://doi.org/10.1016/j.resconrec.2010.04.001.

Commission, N. D. A. R. (2014). Annual Report of Comprehensive Utilization of Resources in China. *(in Chinese)*.

Ecoivent (2020). The Life Cycle Inventory Data Version 3.7. [Online]. Swiss Centre for Life Cycle Inventories. https://www.ecoinvent.org/database/ecoinvent-371/ecoinvent-37/ecoinvent-37.html.

ESMA (2021). Preliminary Report - Emission Allowances and Derivatives Thereof. [Online]. https://www.esma.europa.eu/sites/default/files/library/esma70-445-7_preliminary_report_on_emission_allowances.pdf.

Gómez-Casero, M.A., Pérez-Villarejo, L., Castro, E., and Eliche-Quesada, D. (2021). Effect of steel slag and curing temperature on the improvement in technological properties of biomass bottom ash based alkali-activated materials. Constr. Build. Mater. *302*, 124205. https://doi.org/10.1016/j.conbuildmat.2021.124205.

Greeshma, G., Kyle, F., Sung-Hwan, J., and Ah-Hyung, A.P. (2015). Carbonation of silicate minerals and industrial wastes and their potential use as sustainable construction materials. Advances in CO2 Capture, Sequestration, Conversion *1194*, 295–322. https://doi.org/10.1021/bk-2015-1194.ch012.

Guo, R., Chen, Q., Huang, H., Hu, X., and Wang, T. (2019). Carbonation curing of industrial solid waste-based aerated concretes. Greenhouse Gases: Sci. Technol. *9*, 433–443. https://doi.org/10.1002/ghg.1862.

He, Z., Shen, A., Lyu, Z., Li, Y., Wu, H., and Wang, W. (2020). Effect of wollastonite microfibers as cement replacement on the properties of cementitious composites: a review. Constr. Build. Mater. *261*, 119920. https://doi.org/10.1016/j.conbuildmat.2020.119920.

Huang, H., Guo, R., Wang, T., Hu, X., Garcia, S., Fang, M., Luo, Z., and Maroto-Valer, M.M. (2019a). Carbonation curing for wollastonite-Portland cementitious materials: CO2 sequestration potential and feasibility assessment. J. Clean. Prod. *211*, 830–841. https://doi.org/10.1016/j.jclepro.2018.11.215.

Huang, H., Wang, T., Kolosz, B., Andresen, J., Garcia, S., Fang, M., and Maroto-Valer, M.M. (2019b). Life-cycle assessment of emerging CO2 mineral carbonation-cured concrete blocks: comparative analysis of CO2 reduction potential and optimization of environmental impacts. J. Clean. Prod. *241*, 118359. https://doi.org/10.1016/j.jclepro.2019.118359.

Huijgen, W.J.J., Comans, R.N.J., and Witkamp, G.-J. (2007). Cost evaluation of CO2 sequestration by aqueous mineral carbonation. Energy Convers. Manag. *48*, 1923–1935. https://doi.org/10.1016/j.enconman.2007.01.035.

Huijgen, W.J.J., Ruijg, G.J., Comans, R.N.J., and Witkamp, G.-J. (2006). Energy consumption and net CO2Sequestration of aqueous mineral carbonation. Ind. Eng. Chem. Res. *45*, 9184–9194. https://doi.org/10.1021/ie060636k.

IEA (2013). Mineralisation - Carbonation and Enhanced Weathering.

Jang, J.G., Kim, G.M., Kim, H.J., and Lee, H.K. (2016). Review on recent advances in CO2 utilization and sequestration technologies in cement-based materials. Constr. Build. Mater. *127*, 762–773. https://doi.org/10.1016/j.conbuildmat.2016.10.017.

Khan, R.I., Ashraf, W., and Olek, J. (2021). Amino acids as performance-controlling additives in carbonation-activated cementitious materials. Cement Concrete Res. *147*, 106501. https://doi.org/10.1016/j.cemconres.2021.106501.

Kim, T., Tae, S., and Roh, S. (2013). Assessment of the CO2 emission and cost reduction performance of a low-carbon-emission concrete mix design using an optimal mix design system. Renew. Sustain. Energy Rev. *25*, 729–741. https://doi.org/10.1016/j.rser.2013.05.013.

Li, Q., Zhang, L., Gao, X., and Zhang, J. (2020a). Effect of pulverized fuel ash, ground granulated blast-furnace slag and CO2 curing on performance of magnesium oxysulfate cement. Constr. Build. Mater. *230*, 116990. https://doi.org/10.1016/j.conbuildmat.2019.116990.

Li, X., Bertos, M.F., Hills, C.D., Carey, P.J., and Simon, S. (2007). Accelerated carbonation of

municipal solid waste incineration fly ashes. Waste Manag. *27*, 1200–1206. https://doi.org/10.1016/j.wasman.2006.06.011.

Li, Z., Liu, J., Xiao, J., Zhong, P., and Wang, J. (2020b). Drying shrinkage of mortar manufactured with recycled fine aggregate at vary initial saturation degree. Constr. Build. Mater. *264*, 120621. https://doi.org/10.1016/j.conbuildmat.2020.120621.

Liang, C., Pan, B., Ma, Z., He, Z., and Duan, Z. (2020). Utilization of CO2 curing to enhance the properties of recycled aggregate and prepared concrete: a review. Cem. Concr. Compos. *105*, 103446. https://doi.org/10.1016/j.cemconcomp.2019.103446.

Liu, W., Teng, L., Rohani, S., Qin, Z., Zhao, B., Xu, C.C., Ren, S., Liu, Q., and Liang, B. (2021). CO2 mineral carbonation using industrial solid wastes: a review of recent developments. Chem. Eng. J. *416*, 129093. https://doi.org/10.1016/j.cej.2021.129093.

López-Arce, P., Gómez-Villalba, L.S., Martínez-Ramírez, S., Álvarez De Buergo, M., and Fort, R. (2011). Influence of relative humidity on the carbonation of calcium hydroxide nanoparticles and the formation of calcium carbonate polymorphs. Powder Technol. *205*, 263–269. https://doi.org/10.1016/j.powtec.2010.09.026.

Mo, L., Zhang, F., and Deng, M. (2016). Mechanical performance and microstructure of the calcium carbonate binders produced by carbonating steel slag paste under CO 2 curing. Cem. Concr. Res. *88*, 217–226. https://doi.org/10.1016/j.cemconres.2016.05.013.

Monkman, S., and Shao, Y. (2006). Assessing the carbonation behavior of cementitious materials. J. Mater. Civil Eng. *18*, 768–776. https://doi.org/10.1061/(ASCE)0899-1561.

NASA (2012). Technology Readiness Level. [Online]. https://www.nasa.gov/directorates/heo/scan/engineering/technology/technology_readiness_level.

Ning, J., Liu, A., and Ye, Z. (2020). In China statistical yearbook 2020, C.S. Press, ed. (Beijing).

Pan, S.-Y., Chang, E.E., and Chiang, P.-C. (2012). CO2 capture by accelerated carbonation of alkaline wastes: a review on its principles and applications. Aerosol Air Qual. Res. *12*, 770–791. https://doi.org/10.4209/aaqr.2012.06.0149.

Sanna, A., Uibu, M., Caramanna, G., Kuusik, R., and Maroto-Valer, M.M. (2014). A review of mineral carbonation technologies to sequester CO2. Chem. Soc. Rev. *43*, 8049–8080. https://doi.org/10.1039/c4cs00035h.

Tang, P., Xuan, D., Cheng, H.W., Poon, C.S., and Tsang, D.C.W. (2020). Use of CO2 curing to enhance the properties of cold bonded lightweight aggregates (CBLAs) produced with concrete slurry waste (CSW) and fine incineration bottom ash (IBA). J. Hazard Mater. *381*, 120951. https://doi.org/10.1016/j.jhazmat.2019.120951.

Union_Engineering (2016). Cost Effective Solution for Oil & Gas. [Online]. The United Kindom: Union engineering. https://union.dk/news-pr/all-news/cost-effective-solution-for-oilgas/.

Vandeperre, L.J., and Al-Tabbaa, A. (2007). Accelerated carbonation of reactive MgO cements. Adv. Cem. Res. *2*, 67–79. https://doi.org/10.1680/adcr.2007.19.2.67.

Wang, D., Noguchi, T., and Nozaki, T. (2019). Increasing efficiency of carbon dioxide sequestration through high temperature carbonation of cement-based materials. J. Clean. Prod. *238*, 117980. https://doi.org/10.1016/j.jclepro.2019.117980.

Wang, L., Chen, L., Provis, J.L., Tsang, D.C.W., and Poon, C.S. (2020). Accelerated carbonation of reactive MgO and Portland cement blends under flowing CO2 gas. Cem. Concr. Compos. *106*, 103489. https://doi.org/10.1016/j.cemconcomp.2019.103489.

Wang, T., Huang, H., Hu, X., Fang, M., Luo, Z., and Guo, R. (2017). Accelerated mineral carbonation curing of cement paste for CO 2 sequestration and enhanced properties of blended calcium silicate. Chem. Eng. J. *323*, 320–329. https://doi.org/10.1016/j.cej.2017.03.157.

Wang, T., Yi, Z., Guo, R., Huang, H., Garcia, S., and Maroto-Valer, M.M. (2021). Particle carbonation kinetics models and activation methods under mild environment: the case of calcium silicate. Chem. Eng. J. *423*, 130157. https://doi.org/10.1016/j.cej.2021.130157.

Wang, X.-Y. (2020). Design of low-cost and low-CO2 air-entrained fly ash-blended concrete considering carbonation and frost durability. J. Clean. Prod. *272*, 122675. https://doi.org/10.1016/j.jclepro.2020.122675.

Wei, Z., Wang, B., Falzone, G., La Plante, E.C., Okoronkwo, M.U., She, Z., Oey, T., Balonis, M., Neithalath, N., Pilon, L., and Sant, G. (2018). Clinkering-free cementation by fly ash carbonation. J. CO2 Util. *23*, 117–127. https://doi.org/10.1016/j.jcou.2017.11.005.

Xie, H., Tang, L., Wang, Y., Liu, T., Hou, Z., Wang, J., Wang, T., Jiang, W., and Were, P. (2016). Feedstocks study on CO2 mineralization technology. Environ. Earth Sci. *75*, 615. https://doi.org/10.1007/s12665-016-5352-8.

Xie, H., Yue, H., Zhu, J., Liang, B., Li, C., Wang, Y., Xie, L., and Zhou, X. (2015). Scientific and engineering progress in CO 2 mineralization using industrial waste and natural minerals. Engineering *1*, 150–157. https://doi.org/10.15302/j-eng-2015017.

Yi, Z., Wang, T., and Guo, R. (2020). Sustainable building material from CO2 mineralization slag: aggregate for concretes and effect of CO2 curing. J. CO2 Util. *40*, 101196. https://doi.org/10.1016/j.jcou.2020.101196.

Zhan, B., Poon, C., and Shi, C. (2013). CO2 curing for improving the properties of concrete blocks containing recycled aggregates. Cem. Concr. Compos. *42*, 1–8. https://doi.org/10.1016/j.cemconcomp.2013.04.013.

Zhan, B., Poon, C., and Shi, C. (2016). Materials characteristics affecting CO2 curing of concrete blocks containing recycled aggregates. Cem. Concr. Compos. *67*, 50–59. https://doi.org/10.1016/j.cemconcomp.2015.12.003.

Zhan, B., Poon, C.S., Liu, Q., Kou, S., and Shi, C. (2014). Experimental study on CO2 curing for enhancement of recycled aggregate properties. Constr. Build. Mater. *67*, 3–7. https://doi.org/10.1016/j.conbuildmat.2013.09.008.

Zhang, Z., Pan, S.-Y., Li, H., Cai, J., Olabi, A.G., Anthony, E.J., and Manovic, V. (2020). Recent advances in carbon dioxide utilization. Renew. Sustain. Energy Rev. *125*, 109799. https://doi.org/10.1016/j.rser.2020.109799.

STAR★METHODS

KEY RESOURCES TABLE

REAGENT or RESOURCE	SOURCE	IDENTIFIER
Deposited data		
CO_2 emission factor (Coking coal, Default)	2006 IPCC Guidelines for National Greenhouse Gas Inventories	https://www.ipcc-nggip.iges.or.jp/public/2006gl/index.html
CO_2 emission factor (Diesel oil, Default)	2006 IPCC Guidelines for National Greenhouse Gas Inventories	https://www.ipcc-nggip.iges.or.jp/public/2006gl/index.html
Cement CO_2 emission (GWP)	The Life Cycle Inventory Data Version 3.7 - ecoinvent	https://www.ecoinvent.org/database/
Electric power CO_2 emission in Henan province, China (GWP)	The Life Cycle Inventory Data Version 3.7 - ecoinvent	https://www.ecoinvent.org/database/
Electricity price in Henan province, China	State Grid Henan Electric Power Company	http://www.ha.sgcc.com.cn/
Labor price in Henan province, China	People's Government of Henan Province	https://www.henan.gov.cn/
Cost of CO_2 capture by pressure swing adsorption process	UNION_ENGINEERING. 2016. COST EFFECTIVE SOLUTION FOR OIL & GAS. The United Kingdom: Union engineering.	https://union.dk/news-pr/all-news/cost-effective-solution-for-oilgas/
European Union Allowance	Preliminary report - Emission Allowances and derivatives thereof	https://www.esma.europa.eu/sites/default/files/library/esma70-445-7_preliminary_report_on_emission_allowances.pdf
[Database]: [Dataset for "An Industrial Demonstration Study on CO_2 Mineralization Curing for Concrete"]	Mendeley Data https://doi.org/10.17632/7x27pg63hd.1	https://data.mendeley.com/datasets/7x27pg63hd/1
Software and algorithms		
Reaction enthalpy database	HSC Chemistry	Metso Outotec
Compressibility factor of CO_2 (PRSK, pure substance, and UNIFACmodel)	Aspen 8.0 property database	Aspentech
Microsoft Excel	Microsoft	Excel v.16.0

RESOURCE AVAILABILITY

Lead contact

Further information and requests for resources should be directed to and will be fulfilled by the lead contact, Tao Wang (oatgnaw@zju.edu.cn).

Materials availability

This study did not generate new unique reagents.

Data and code availability

All original data has been deposited at Mendeley Data and is publicly available as of the date of publication. DOI is listed in the key resources table.

METHOD DETAILS

Raw materials

The filler powder was made up of a 5:4:1 mixture of waste slag, waste ash, and cement. Steel slag was delivered by Henan Jiyuan Iron & Steel Co. LTD., located 75 km away from the demonstration base. The steel manufacturing method was converter steelmaking with water quenching. Blaster furnace slag and fly ash were supplied by Jiaozuo Wanfang Electric Power Co., LTD, located 25 km away from the base. Carbide

slag was a by-product of calcium carbide obtained from Henan Lianchuang Chemical Co. LTD., located 70 km away from the base. P.O. 42.5 cement from Jiaozuo Qianye Cement Co. LTD. (30 km away) was used for filler preparation. CO_2 was purchased from Henan Xinlianxin Fertilizer Co. LTD., in the form of a liquid with a purity of more than 90%, transported by tanker. The particle size distribution of waste slag and waste ash were shown in Table S7 and Figure S1 respectively, and the element composition of the above raw materials are listed in Table S8.

Physicochemical characterization

The microstructure and morphology of the samples were comprehensively characterized through Scanning electron microscopy (SEM), X-ray diffraction (XRD), and Thermogravimetry (TG) tests. The samples were sprayed with gold for 2 minutes before the SEM test (SU-3500, Hitachi). The CuKα radiation PANalytical X-ray diffractometer was used for XRD analysis with 2θ° from 10° to 70°. Jade 5.0 was used to process curves and determine peaks. The powder sample was taken from the surface of the specimen. The carbonation degree of bricks was determined using TG/DSC (NETZSCH STA 449 F3). The operating temperature ranges between 10 and 1000°C, with a 10°C/min heating rate and a nitrogen flow rate of 50 mL/min. The weight loss between 400-800°C was attributed to the decarbonation of metastable $CaCO_3$ (particularly, amorphous calcium carbonate and vaterite) and decrystallization of calcite and aragonite (Khan et al., 2021). The element composition of raw materials was determined by an X-ray Fluorescence spectroscope (XRF, Shimadzu Corporation, XRF-1800).

QUANTIFICATION AND STATISTICAL ANALYSIS

Calculating methods

CO_2 conversion rate

The CO_2 conversion rate, C, is calculated from Equation 3, where, m_{in} and m_{out} denote the inlet and outlet CO_2 gas mass, respectively. The inlet gas mass was determined by weighing the liquid CO_2 trunk over the weighbridge. The outlet CO_2 mass was calculated by Equation 4, where, p and T denote the pressure (Pa) and temperature (K) after CO_2 curing in the chambers, respectively; V denotes the volume of the curing chamber (m^3); M_{CO2} denotes the molar mass of CO_2 (g/mol); z denotes the compressibility factor of CO_2 obtained from Aspen 8.0 property database (PRSK, pure substance, and UNIFAC model). R denotes the gas constant, which is 8.314 m^3/(mol·K).

$$C = (m_{in} - m_{out})/m_{in} \quad \text{(Equation 3)}$$

$$m_{out} = \sum \frac{M_{CO2} \times pV}{zRT} \quad \text{(Equation 4)}$$

CO_2 uptake during curing process

The real-time change of CO_2 uptake C_t (wt %) in chambers during the CO_2 curing process is calculated by Equation 5, where, Q denotes the average CO_2 flow from a Vortex shedding flowmeter (VSF) in the front of gas separate cylinder (ton/min); p_t and T_t denote the gauge pressure (Pa) and temperature (K) at time t in the chambers, respectively. p_s denotes the saturation pressure of steam at T_t (Pa).

$$C_t = Q \times t - \frac{M_{CO2} \times (p_t - p_s)V}{zRT_t} \quad \text{(Equation 5)}$$

The CO_2 uptake C_t (wt %) in the next chambers in the PE stage is calculated by Equation 6. p_1 and T_1 denote the gauge pressure (Pa) and temperature (K) in the finished chambers at the initial time t_0, respectively. p_{1t} and p_{2t} denotes the pressures at time t in the finished chambers and the next chambers (Pa), respectively; T_{1t} and T_{2t} denotes the temperatures at time t in the finished chambers and the next chambers (K), respectively; p_{s1}, p_{s1t}, and p_{s2t} denote the saturation pressure (Pa) of steam at T_1, T_{1t} and T_{2t}, respectively (Because of the cooling effect of the PE, liquid water is continuously separated so that the humidity in the chambers is kept at saturation levels).

$$C_t = \left(\frac{p_1 - p_{s1}}{z_1 RT_1} - \frac{p_{1t} - p_{s1t}}{z_1 RT_{1t}} - \frac{p_{2t} - p_{s2t}}{z_2 RT_{2t}}\right) \times V \times M_{CO2} \quad \text{(Equation 6)}$$

CO_2 mineralization reaction heat

CO_2 mineralization reaction heat E (kJ/100g-material) is obtained by Equation 7. ΔH_i denotes theoretical enthalpy change (from HSC CHEMISTRY 6.0 database in Table S3) of hydroxide i (corresponding to oxide i)

in reaction with CO_2 (kJ/mol); C_d denotes the CO_2 uptake of dry raw materials (g-CO_2/100 g-material); M_{CO2} denotes the molar mass of CO_2 (g/mol); N denotes the total amount of substance of activated oxide in 100 g raw material; N_i denotes the amount of substance of activated oxide i.

N_i is calculated by Equation 8, where, λ_j denotes the proportion of raw material j (%); $\omega_{j,i}$ denotes the the proportion of active oxide i in dry raw material j (%); M_i denotes the molar mass active oxide i (g/mol). Here, i represents CaO, MgO, K_2O, and Na_2O; j represents steel slag, furnace blaster slag, fly ash, carbide slag, and cement, respectively. The oxide proportion is referred from Table S8.

$$E = \sum_{i=1}^{n} \Delta H_i \times \frac{C_d \times N_i}{M_{CO2} \times N} \quad \text{(Equation 7)}$$

$$N_{CaO} = \sum_{j=1}^{n} \lambda_j \times \left(\omega_{j,CaO} - 0.7 \times \omega_{j,SO3} - \omega_{j,CaO(carbonate)}\right) \Big/ M_{CaO}$$

$$N_{MgO} = \sum_{j=1}^{n} \lambda_j \times \omega_{j,MgO} \Big/ M_{MgO}$$

$$N_{K2O} = \sum_{j=1}^{n} \lambda_j \times \omega_{j,K2O} \Big/ M_{K2O} \quad \text{(Equation 8)}$$

$$N_{Na2O} = \sum_{j=1}^{n} \lambda_j \times \omega_{j,Na2O} \Big/ M_{Na2O}$$

Compressive strength

The uniaxial compressive strength of brick samples under natural curing and CO_2 curing were tested using the universal tester, with a precision of 0.1 MPa. In the present study, the compressive strength after CO_2 curing and natural curing were tested after 3d, 7d, 28d and 45d hydration in air. The displacement control was set to the universal tester with a loading speed of 2mm/min. The compressive strength is calculated by Equation 9, where, R_c and F_c denote the compressive strength (MPa) and the peak load (kN) when the sample is destroyed, respectively; A denotes the area (mm^2) of the sample compression surface. The ultimate strength is the average value of one group of three parallel specimens for each condition.

$$R_c = F_c/A \quad \text{(Equation 9)}$$

Calculation of LCI

Mixture design

The mixture design was used to compare the GWP difference between CO_2 curing and autoclaved curing (Table S9). Considering the original working condition of autoclaved curing, the steam consumption was approximately 45 kg/m^3-concrete (8.7 m^3-steam/m^3-concrete with 180°C and 1 MPa, the density = 5.16 kg/m^3).

Functional units

Ecoinvent v3.7 was used to obtain basic unit data and to calculate LCI. Based on variations in manufacturing processes, energy requirements for mixing, crushing, and molding processes as well as other plant energy requirements were obtained from the electricity functional unit (power plant). The corresponding mechanical energy consumed during the transportation of raw materials was obtained from the diesel functional unit (diesel engine); the energy consumed in steam heating during the autoclaved curing process came from the coal-fired functional unit (boiler). The electric power emission data was obtained from the ecoinvent database, according to the power source in Henan province, China; coal and diesel were based on global average emissions. In the actual operation, the curing chamber exhibited good thermal insulation as well as pressure holding performance, and no additional energy was input for pressure and temperature control (CCP and CCT are 0).

Calculation of GWP

The GWP indices were calculated as:

$$I_{GWP} = IR_{GWP} + IM_{GWP} + IT_{GWP} \quad \text{(Equation 10)}$$

$$IR_{GWP} = \sum_{i=1}^{n}(W_i \cdot IR_{i,GWP}) \quad \text{(Equation 11)}$$

$$IM_{GWP} = \sum_{j=1}^{n}(IM_{j,GWP}) - C \quad \text{(Equation 12)}$$

$$IT_{GWP} = \sum_{i=1}^{n}(W_i \cdot D_i \cdot IT_{i,GWP}) \quad \text{(Equation 13)}$$

Whereby, in Equation 10, I_{GWP} represents the GWP index value; IR_{GWP}, IM_{GWP}, and IT_{GWP} respectively denote the evaluation data of the raw materials unit, manufacture unit, and transportation unit; i and j respectively represent different orders of raw material types and manufacture processes. In Equation 11, W_i and $IR_{i,GWP}$ represent the mass (kg-material/m^3) and GWP-LCI values of raw materials i (kg-CO_2/kg-material); In Equation 12, $IM_{j,GWP}$ represents the GWP-LCI value of manufacture step j (kg-CO_2/m^3), while C denotes CO_2 uptake pre unit concrete product (kg-CO_2/m^3); In Equation 13, D_i represents the transportation distance of raw material i (km), while $IT_{i,GWP}$ represents the GWP-LCI index value for raw material I, transported by freight vehicles (kg-CO_2/(kg-material· km)).

Allocations

With regards to raw materials, production data of Portland-cement was obtained from the ecoinvent database, according to the the cut-off by classification principle. To determine the potential environmental benefits of solid wastes (waste slag and ash in this study) utilization, the "allocation by economic value" is used to calculation the GWP. The result showed the allocation coefficient of waste is no more than 5% (2.3% for slag and 1% for ash) (Chen et al., 2010), so that the GWP of solid waste (~10^{-2} kg-CO_2/Eq) is neglected in this study. The gas source was a liquid CO_2 tank truck with 99% purity. Given that CO_2 gas compression and purification were necessary processes in CO_2 capture, in this study, the relevant energy consumption was not included in the life cycle boundary. With regards to transportation, freight vehicle was set as the standard loading capacity with 32 t, and diesel fuel consumption for 100 kilometers was 32 L. It was assumed that CO_2 was transported through pipelines without quality and economic allocation. During the manufacturing processes, we took the electric power consumption (averaged to per cubic product) of the whole plant when operating at full load for the two curing processes. The GWP calculation are shown in Table S5.

Calculation of economic benefit

Life cycle cost (C_{LCC}) was calculated as:

$$C_{LCC} = C_{Raw\ material} + C_{Manufacture} + C_{Gas\ supply} + C_{Labor} \quad \text{(Equation 14)}$$

$$C_i = \sum_{j=1}^{n}(W_j \cdot P_j) \quad \text{(Equation 15)}$$

whereby, in Equation 14, C_{LCC} represents the LCC of CMC; $C_{Raw\ material}$, $C_{Manufacture}$, $C_{Gas\ supply}$, and C_{Labor} are the costs of raw materials unit, manufacture unit, gas supply unit, as well as labor unit, respectively. In Equation 15, i and j respectively represent different orders of process types and index types; W_j and P_j denote the functional value and the price of index j. The calculations and units are shown in Table S6.